JOURNAL OF APPLIED ELECTROCHEMISTRY 25 (1995) 781–791

Effect of the addition of Cr and Nb on the microstructure and electrochemical corrosion of heat-treatable Al–Zn–Mg alloys

P. L. CABOT, J. A. GARRIDO, E. PÉREZ

Departament de Química Física, Facultat de Química, Universitat de Barcelona, Martí i Franquès 1, 08028 Barcelona, Spain

A. H. MOREIRA, P. T. A. SUMODJO

Departamento de Química Fundamental, Instituto de Química, USP, Cidade Universitaria, Caixa Postal 20780, CEP 01498, São Paulo, SP, Brazil

A. V. BENEDETTI

Departamento de Físico-Química, Instituto de Química, UNESP, Caixa Postal 355, CEP 14800, Araraquara, SP, Brazil

Received 9 September 1994; revised 12 January 1995

The effect of the addition of Cr and Nb on the microstructure and the electrochemical corrosion of the weldable, high-strength and stress corrosion cracking (SCC) resistant Al–5%Zn–1.67%Mg–0.23%Cu alloy (H) has been studied. Combined additions of the alloying elements, J (with Nb), L (with Cr) and O (with Cr and Nb) and different heat treatments, ST (cold-rolled), A (annealed), F (quenched), B (quenched and aged) and C (quenched in two steps and aged), to obtain different microstructures and hardness have been performed. To correlate the electrochemical corrosion with the microstructure of the specimens, corrosion potential (E_{cor}) measurements in different chloride solutions were performed and optical microscopy, SEM, TEM and EDX were applied. In chloride solutions containing dissolved O_2 or H_2O_2, the present alloys were polarized up to the pitting attack. It was shown that the E_{cor} measurements were very sensitive to the alloy composition and heat treatment, increasing in the order H < J < L < O < Al (for a given heat treatment) and F < A ≈ ST < B < C (for a given alloy). The $MgZn_2$ precipitates of the annealed (A) and cold-rolled (ST) specimens were dissolved in chloride solutions containing oxidizing agents and pitting attack was shown to develop in the cavities where the precipitates were present. In the specimens B and C, the compositions of the precipitate free zones was found to be equal to that of the matrix solid solution and preferential intergranular attack was not evident, this being in agreement with their SCC resistance. The addition of Cr and Nb increased the pitting corrosion resistance. The effects of Cr and Nb were additive, that of Cr being predominant, either, in the E_{cor} shift or in the increase in the pitting corrosion resistance.

1. Introduction

Al–Zn–Mg alloys are age-hardenable, low-density, weldable and corrosion resistant materials which are mainly used for constructional purposes [1]. Many studies using small additions of different alloying elements have been performed because of their technological interest and their susceptibility to stress corrosion cracking (SCC) under certain conditions [1–9]. The addition of 0.15–0.25% Cr and 0.15–0.29% Cu was recommended for a SCC resistant, high-strength and weldable Al–(4.9–5.2%)Zn–(1.6–1.8%)Mg alloy [6]. The addition of Nb has only recently been considered [10, 11]. These results show that Nb addition increases the fatigue resistance of the alloy, slightly reduces its grain size and produces a small shift of the corrosion, breakdown and repassivation potentials in the positive direction.

Anodic dissolution and hydrogen embrittlement theories have been proposed to interpret the SCC of Al alloys. The anodic dissolution theory explains the experimental finding that SCC takes place with the preferential dissolution of the grain boundary (GB) precipitates and the precipitate free zone (PFZ) [3, 8, 12]. On the other hand, the hydrogen embrittlement theory explains the similar dependence of SCC susceptibility and of hydrogen permeation with potential, the reduction in tensile ductility after exposure to humid environments, the change in the SCC susceptibility with loading mode and the effect of the hydrogen recombination poisons [13, 14]. Scamans *et al.* [14] and H.-P. Kim *et al.* [13] suggested that

0021-891X

Table 1. Compositions of the Al–Zn–Mg alloys under study, given in wt %

Alloy	*Zn*	*Mg*	*Cu*	*Cr*	*Nb*	*Si*	*Ti*
H	5.03	1.67	0.23	<0.001	<0.010	0.006	<0.001
J	5.00	1.66	0.23	<0.001	0.053	0.006	<0.001
L	4.98	1.65	0.24	0.140	<0.010	0.007	<0.001
O	4.98	1.63	0.24	0.140	0.053	0.001	0.003

hydrogen embrittlement is involved in the SCC of the Al–Mg, Al–Zn–Mg and Al–Zn–Mg–Cu alloys, the Mg segregated to the GBs presenting a critical role. In the anodic dissolution theory, the susceptibility to the intergranular and stress corrosion is ascribed to the more anodic breakdown potential of the region near the GBs when compared with the breakdown potential of the matrix solid solution [12]. As the Mg segregation to the GBs can make the breakdown potential of the GB region more anodic, the final cause of SCC is still controversial.

The utility of potentiostatic and potentiodynamic methods to study the intergranular corrosion and to predict the SCC susceptibility of Al–4%Cu, Al–6%Zn–2.5%Mg–1.7%Cu–0.2%Cr(7075) and Al–5%Zn–1.7%Mg–0.2%Cu (alloy H) has been demonstrated in previous works [3, 8, 12, 15, 16]. Maitra and English [8] and Byrne [3] explained the decrease in the SCC susceptibility of differently heat-treated 7075 Al–Zn–Mg alloys by the Cu depletion of the matrix solid solution, this causing the breakdown potential of the matrix solid solution to approach the breakdown potential of the GBs. EDX microanalysis demonstrated the Cu incorporation in the $MgZn_2$ precipitates after different heat treatments [3, 15]. On the other hand, the SCC resistance of the age-hardened alloy H [7] was related with the very small charge of the anodic maximum appearing in the cyclic voltammograms [16].

Despite microstructure, mechanical characteristics and SCC resistance of Al–Zn–Mg alloys with different contents in Zn and Mg having been widely studied in the literature, only few works deal with their electrochemistry. In this work, the relation between the microstructure and the corrosion behaviour of alloys having the composition of alloy H with combined additions of Cr and Nb and submitted to different heat treatments is studied using open circuit potential (o.c.p.) against time measurements, ASTM standard measurements of corrosion potential, optical microscopy, SEM, TEM and EDX. The results are compared with previous SEM and electrochemical data obtained for alloy H. The corrosion potentials are the first essential data in characterizing the anodic character and microstructure of Al alloys [1].

2. Experimental details

2.1. *Preparation of the specimens*

The specimens were prepared following the same procedure as for alloy H [15]. The composition of the alloys, named H, J, L and O, were determined by spectrographic analysis, the corresponding results being listed in Table 1. The Fe, Ni, V and Mn contents were found to be less than 0.001%. The alloy specimens were cut from the final cold-rolled sheet (0.4 cm in thickness) as cylinders having 3 mm diameter, and afterwards, they were submitted to the different heat treatments, ST, A, F, B and C, as previously described [7, 15, 16]. The corresponding treatment sequences have been summarized in Table 2.

Table 2. Synopsis of the heat treatments of the Al–Zn–Mg alloys

*Treatment sequence**	*ST*	*A*	*F*	*B*	*C*
In common: casting + 500 °C, 4 h + hot rolling (1 cm) + cold-rolling (0.4 cm)†					
Solution treatment at 480 °C	–	24 h	1 h	1 h	1 h
Slow cooling rate	–	for 48 h	–	–	–
Quenching stop in salt bath at 400 °C	–	–	–	–	2 min
Quenching in water at 10 °C	–	–	×	×	×‡
Ageing: 3 days 25 °C + 8 h, 90 °C + 24 h, 135 °C	–	–	×	×	×

* The treatment sequence was always in the order given in the left column. × means yes and the dash means that the corresponding treatment was not performed.

† The samples were cut from the final sheet before the following heat treatments.

‡ Quenching from 400 °C after a previous quenching stop at this temperature.

The specimen designation will be given by the symbol relative to its composition followed by the symbol relative to its heat treatment. The high-strength specimens were only those submitted to heat treatments B and C. Only the breaking strains of the specimens HB, HC, LB and LC were previously obtained [7]. These were, respectively, 454 ± 9, 435 ± 2, 480 ± 50 and $478 \pm 10\,MN\,m^{-2}$. After boiling 3.5 h in aqueous solution containing $3\,g\,dm^{-3}$ NaCl + $36\,g\,dm^{-3}$ CrO_3 + $30\,g\,dm^{-3}$ $K_2Cr_2O_7$, the breaking strains were 307 ± 30, 417 ± 20, 355 ± 27 and $353 \pm 24\,MN\,m^{-2}$, also respectively. It was then shown that heat treatment C, based on the theory of the vacancy drag mechanism [17], provided to alloy H better SCC resistance than the direct quenching (heat treatment B), while treatment C did not improve the SCC behaviour of alloy L with respect to treatment B.

2.2. *Electrochemical and microscopical characterization*

The test electrodes were encapsulated in epoxy resin and polished using diamond paste up to 1 μm finish and cleaned with ethanol in ultrasonic bath. Only one base of the alloy cylinder was exposed to the working solution. The electrochemical experiments were performed in a $100\,cm^3$ volume three-electrode cell at 25.0 ± 0.1 °C. The reference and auxiliary electrodes were the SCE, connected via a Luggin capillary, and a platinum wire, respectively. All the potentials given in this work are referred to the SCE. The working electrolytes were NaCl (Merck p.a.) prepared with water which was deionized,

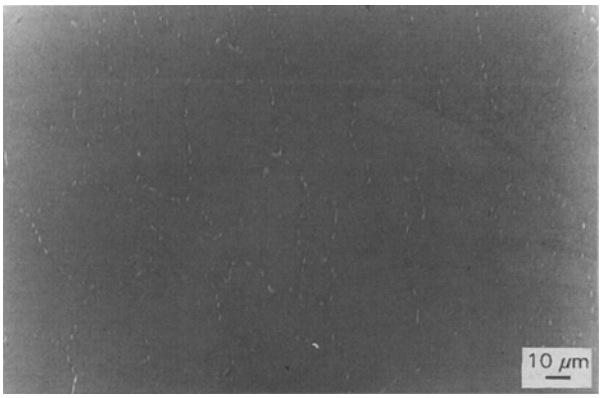

Fig. 1. SEM image of a polished specimen LA.

distilled three times and filtered through a Millipore Milli-Q system.

The electrochemical experiments were performed using a PAR 273 potentiostat and the M342C corrosion software. The open circuit potential (o.c.p.) measurements were conducted in the absence of dissolved oxygen and in oxygen-saturated (1 atm) solutions and following the ASTM G 69-81 'Standard Practice'.

The microstructure of the specimens under study were characterized by means of Keller's etch (concentrated, 3A and diluted, 3B) [18] and a metallographic microscope Olympus PMG3, a Jeol JSM 840 SEM, a STEM Hitachi H-800 and a TEM Hitachi H-8010. The SEM and STEM equipments were furnished with a Link Systems and a Kevex EDX microanalysis system, respectively.

Alloys L and H were prepared to be observed by TEM. In this case, alloy sheets of 1 mm in thickness, cut from the original cold-rolled sheet, were submitted to the corresponding heat treatment. Disks having 3 mm diameter were further prepared using a Gatan 501 ultrasonic cutter. They were then polished up to a thickness of 70 μm and a hollow was further formed in their central part by means of a Dimple Grinder Gatan 656 concave polisher. When the central thickness was reduced to 40 μm, the disc was submitted to an argon sputtering at the temperature of liquid nitrogen.

The specimens were also examined by SEM and EDX before and after the electrochemical experiments. In this case, the test electrodes were rapidly removed from the solution, stirred in benzene to eliminate the solution adhered on the surface, dried and stored under high vacuum.

3. Results and discussion

3.1. *Microstructure of the specimens*

The SEM observation of the polished Al–Zn–Mg alloys showed the existence of small particles in the specimens J, L and O which were submitted to heat treatments A and ST. Such small particles were located principally in the grain boundaries, although they were also found in the grain bodies (Fig. 1). The EDX microanalysis of these particles gave the Mg:Zn stoichiometry of 1:2, this indicating the $MgZn_2$ composition, the intermetallic compound which has also been described in the literature for heat-treated 7075 Al–Zn–Mg [2]. Any precipitates could not be detected by SEM in the specimens submitted to heat treatments F, B and C and the corresponding X-ray mappings showed only a uniform distribution of Mg and Zn along the grains. However, this does not indicate that the specimens F, B and C are necessarily homogeneous, but the possible precipitates can not be detected by this technique. This justifies the TEM examination later reported in this work.

Etching of the polished specimens in 3A (concentrated) and 3B (diluted) Keller's reagents permitted to show the form of the grains, the mean grain size of the specimens and the distribution of the $MgZn_2$ precipitates in the grain. The results of Keller's etch of the specimens O submitted to the different heat treatments are shown in Fig. 2. The mean grain size was much lower in the Cr-containing specimens (see Figs 2 and 8), but was independent of the heat treatment except in the case of heat treatment ST. Contrary, the form of the grains and the distribution of the $MgZn_2$ precipitates essentially depended on the heat treatment.

The specimens ST (Fig. 2(a)) presented elongated grains because of the previous rollings, while polyhedric grains were found for heat treatments A, B, C and F (Fig. 2(b)–(e)). The alloys submitted to heat treatments ST and A presented $MgZn_2$ precipitates in the grain boundaries and in the inner part of the grains (see Fig. 2(a) and (b)). The $MgZn_2$ precipitates in the inner part of the grains of the specimens A were distributed as discontinuous and parallel transgranular bands. The quantity of intragranular $MgZn_2$ precipitates was greater in the specimens LA and OA than in the specimen JA. In the specimens ST, the $MgZn_2$ precipitates were orientated in the direction of the grains. When the specimens A and ST submitted to Keller's etch were observed under the SEM, cavities were found where the $MgZn_2$ precipitates were located.

The GBs of the specimens B and C after Keller's etch appeared to be quite uniform under the metallographic microscope (see Fig. 2(c) and (d)). In addition, the attack in the inner part of the grains was not as localized as in the case of heat treatments A and ST. These results indicate that the $MgZn_2$ precipitates are smaller than those of the latter specimens, in the GBs and also in the grain bodies. More difficult was to observe the GBs of the specimens F by this etching procedure (see Fig. 2(e)). This is consistent with heat treatment F, because quenching leads to $MgZn_2$ precipitates as small as the Guinier–Preston (GP) zones [8].

The results concerning alloys J, L and O, described above, when compared with those previously obtained for alloy H [15], suggest that Nb addition does not produce any significant microstructural

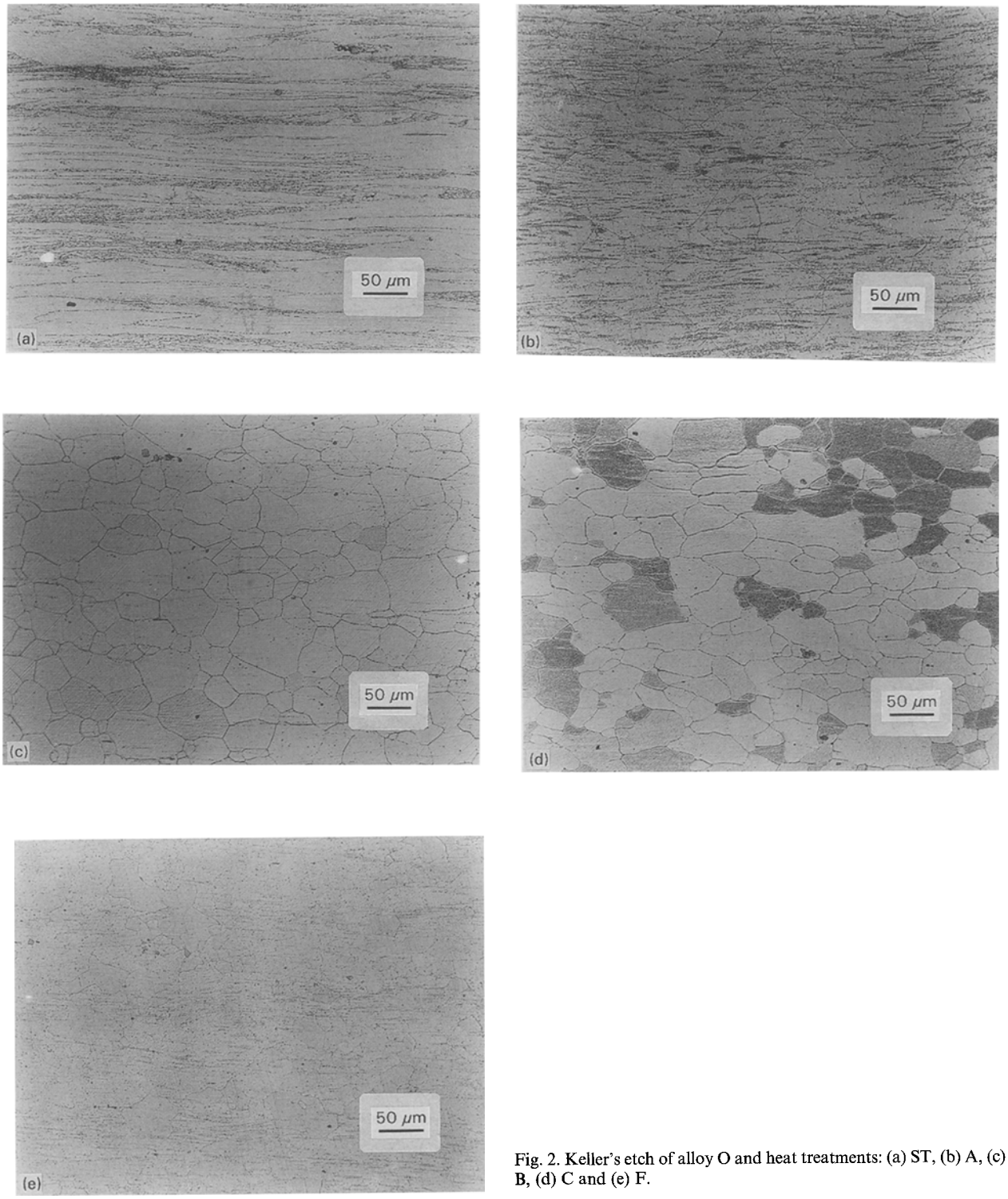

Fig. 2. Keller's etch of alloy O and heat treatments: (a) ST, (b) A, (c) B, (d) C and (e) F.

changes; that is, alloys H and J present very similar microstructures, while Cr addition makes the grain size much smaller.

As shown above, optical microscopy, SEM and EDX were not sufficient to characterize the specimens F, B and C. The $MgZn_2$ precipitates could not be directly observed using these techniques in the latter specimens because they were much smaller than those found in the specimens A and ST. Therefore, TEM, STEM and EDX were used to study the size, distribution and composition of the $MgZn_2$ precipitates along the grains of the specimens having the compositions L and H.

As shown in the TEM micrographs appearing in Fig. 3(a)–(f), the precipitates in all the specimens except F (Fig. 3(f)) were present in the GBs and also in the inner part of the grains. The EDX thin film microanalysis of such precipitates in the STEM observations also indicated the composition of $MgZn_2$, as expected for Al–Zn–Mg alloys having similar contents in Mg and Zn [2–8].

In the specimen LA, the precipitates in the GBs were about 0.4–0.6 μm in length and about 0.2 μm wide, while they were generally a little smaller in the inner part of the grains (Fig. 3(b)). The $MgZn_2$ precipitates in the specimen LST presented similar sizes to those found for the specimen LA, being about 0.2 μm in length and about 0.1 μm wide (Fig. 3(a)). The

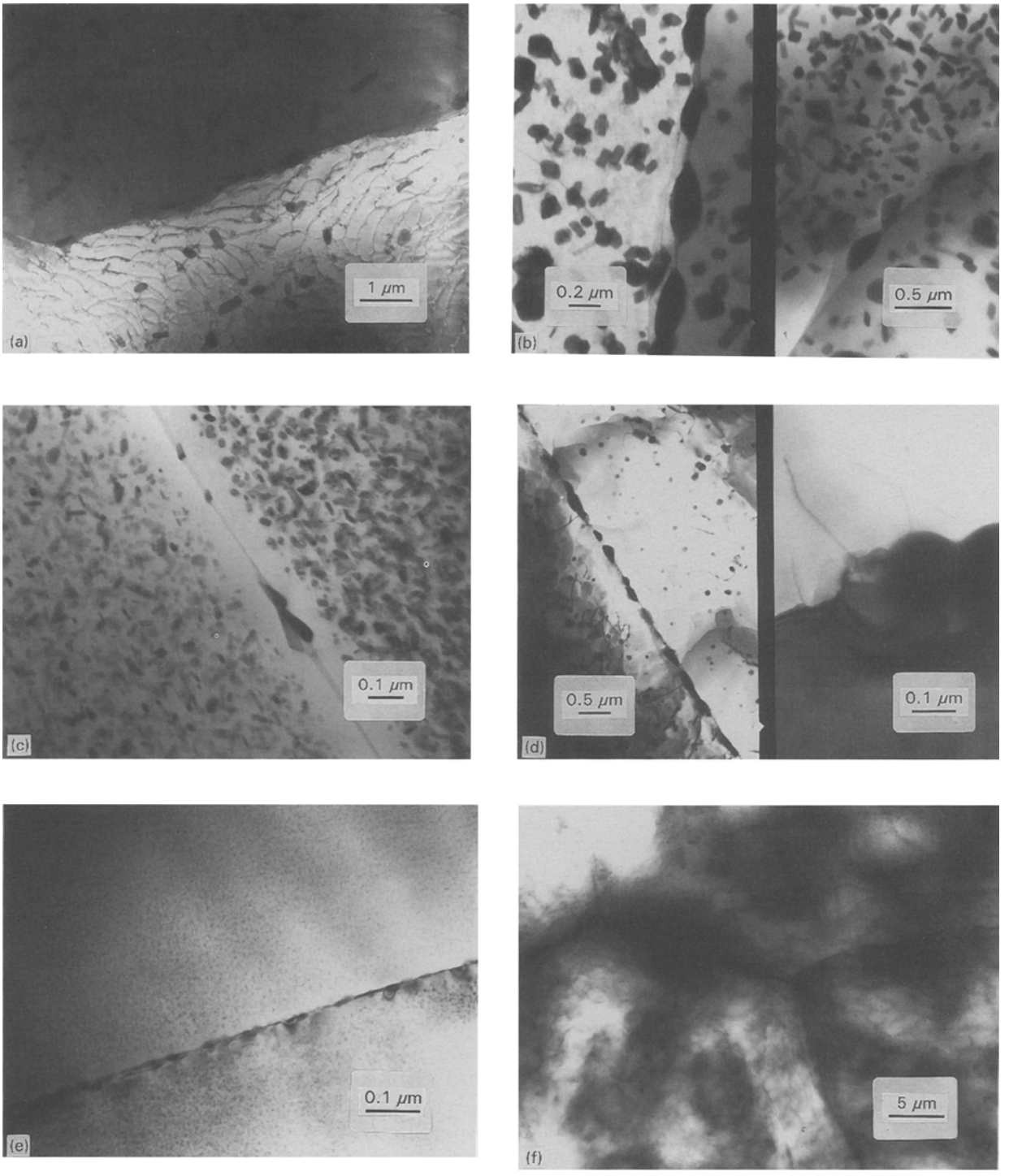

Fig. 3. TEM images of different specimens at different magnifications: (a) LST, (b) LA, (c) LB, (d) HB, (e) LC and (f) LF.

micrographs corresponding to the specimen ST also exhibited many dislocations due to previous rollings.

As shown in Fig. 3(c), the specimen LB presented some $MgZn_2$ precipitate in the GBs, much of it in the inner part of the grains and also a precipitate free zone (PFZ) parallel to the GBs. Such precipitates were also long-shaped but they were much smaller than those found in the specimens LA and LST. The most part of them were about 0.02 μm in length. In addition, a PFZ of about 0.07 μm wide was observed. On the other hand, the size of the precipitates and the width of the PFZ were even smaller for the specimen LC (Fig. 3(e)), while the microstructure of the specimen LF was the most homogeneous (Fig. 3(f)). Precipitates as small as the GP zones [8] and very small and finely dispersed (Al–Cr) nuclei are expected in this latter specimen [6].

Similar results were obtained for alloy H. The TEM, STEM and EDX observations of the specimen HB indicated a lower density of $MgZn_2$ precipitates than in LB and a PFZ of about 0.4 μm wide (Fig. 3(d)).

The thin film microanalysis of the $MgZn_2$ precipitates found in the inner part of the grains and also in the GBs of the specimens submitted to heat

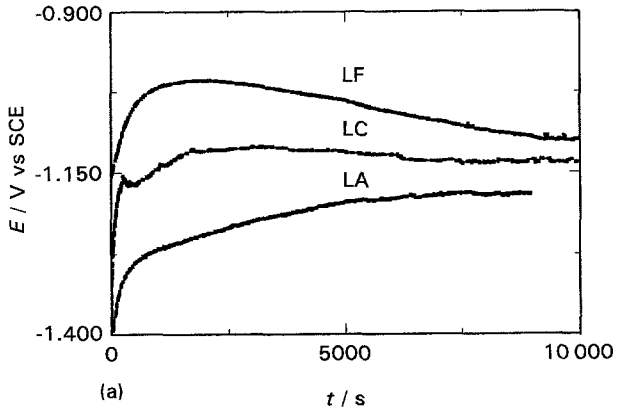

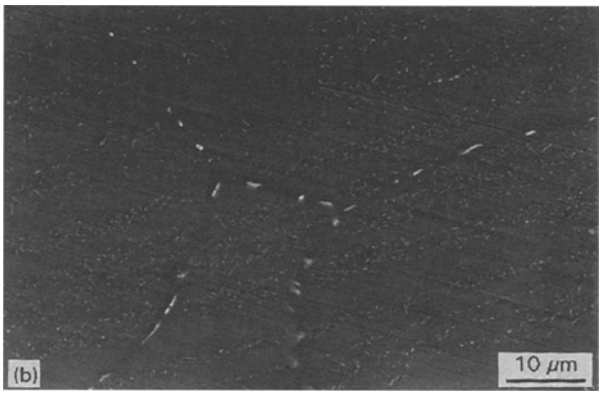

Fig. 4. Effect of deaerated 0.1 M NaCl on different specimens: (a) (o.c.p.) against time measurements of the specimens indicated and (b) SEM image of the specimen LA after immersion in the deaerated solution for 5 h (to be compared with Fig. 1).

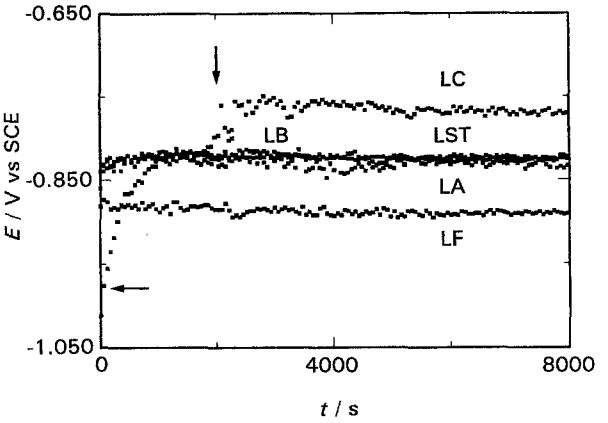

Fig. 5. (O.c.p.) against time measurements for alloy L in oxygen-saturated 0.1 M NaCl. Note that the measurements of LC were initiated in the deaerated solution. Just after the immersion of the specimen into the solution, the cell was opened to the air (horizontal arrow) and afterwards, oxygen was bubbled through the solution (vertical arrow).

treatments A, ST, B and C demonstrated the accumulation of Cu. The presence of Cu in the matrix solid solution and in the PFZ was also demonstrated, although its content was near the detection limit of the EDX microanalysis. The thin film microanalysis also indicated that Cr was present in greater quantity in the $MgZn_2$ precipitates (found in the grains and in the GBs of the specimens LB and LC). The Cr contents in the matrix solid solution and in the PFZ was, as in the case of Cu, near the detection limits of the EDX microanalysis.

The microanalysis of Zn and Mg in the matrix solid solution and in the PFZ was complicated by the small content of these elements in the alloy and the overlapping of the Al and Mg EDX peaks. However, their gaussian deconvolution showed that the Mg and Zn contents of the matrix for the specimens A and ST were similar and also lower than those of specimen F. Thus, the Zn and Mg contents of the solid solution of LA were 3.7 ± 0.4 and $1.5 \pm 0.2\%$, respectively, while those of HST were 4.3 ± 0.7 and $1.5 \pm 0.2\%$ (compare with data shown in Table 1). This agrees with the Zn and Mg depletion of the matrix in favour of the growth of the $MgZn_2$ precipitates when annealing. On the other hand, the composition of the matrix in the specimens B and C was found to have a Zn and Mg content at levels between those of the solid solutions of the specimens A (or ST) and F. In addition, the Zn, Mg, Cu and Cr contents of the PFZ were approximately equal to those found in the matrix solid solution. This is consistent with the characteristics of a SCC resistant Al–Zn–Mg alloy because different compositions in the matrix solid solution and in the PFZ would result in different breakdown potentials and, therefore, to a SCC susceptibility when the most anodic of them corresponds to the GB region.

3.2. *Corrosion potential measurements in O_2-saturated 0.1 M NaCl*

The o.c.p.'s of the specimens in deaerated 0.1 M NaCl varied with time as shown in Fig. 4(a). First, the o.c.p. presented a net shift in the positive direction and afterwards slowly approached a quasisteady value. Such quasisteady values were located in a range from about -1 to -1.2 V for all the specimens studied in this work. The microscopic examination of the specimens, after being immersed for several hours in deaerated 0.1 M NaCl, showed no localized corrosion (see Fig. 4(b) and compare with Fig. 1). The $MgZn_2$ precipitates in the specimens ST and A were still clearly observed under the SEM.

As exemplified in Fig. 4(a), the o.c.p.'s of the specimens F presented small, slow and continuous shifts towards more positive and also towards more negative potentials before approaching the steady state. This was also found for tempers B and C. However, this fluctuation was much less marked for these latter specimens. The general result was that wider fluctuations were found when the size of the precipitates decreased. Such o.c.p. shifts can be explained by the breakdown and repair of the corresponding passive films, which take place at random while the oxide film continuously grow up to reach a constant thickness [19] (the oxide film is very thin just after the immersion). This is in agreement with previous EIS study of alloy J [11]. As less fluctuations are found for specimens having greater precipitates, it is concluded that breakdown zones are easily produced near these precipitates which lead to the evolution of the o.c.p. from more negative potentials (i.e., from

Table 3. Mean quasistatic corrosion potentials (mV vs SCE) of the specimens studied in oxygen-saturated (1 atm) 0.1 M NaCl and following the G 69-81 ASTM Standard Practice (1 M NaCl + 9 ml of 30% H_2O_2 per litre).

Specimen	*O_2-saturated (1 atm) 0.1 M NaCl*	*Standard practice*	*Specimen*	*O_2-saturated (1 atm) 0.1 M NaCl*	*Standard practice*
HST	−860*	−966	LST	−825	−925
HA	−900*	−966	LA	−833	−927
HF		−983	LF	−890	−955
HB	−850*	−887	LB	−825	−860
HC	−800*	−862	LC	−783	−853
JST	−854†	−950	OST	−835	−918
JA	−864†	−957	OA	−833	−923
JF	−900†	−975	OF	−885	−955
JB	−850†	−870	OB	−830	−847
JC	−845†	−860	OC	−820	−848

* Values obtained previously in air-saturated solutions at the atmospheric pressure [15].
† Previously given in [11].

more active states). In contrast, for more homogeneous specimens, transitions between more active and more passive states may appear before reaching the steady state.

The specimens studied presented a very different behaviour when they were immersed in oxygen-saturated (1 atm) 0.1 M NaCl. The o.c.p.'s always evolved in the positive direction and, after a few minutes, they presented sudden, and very frequent, changes in a wide potential range of about ±25 mV or even more, around a mean quasisteady value (Fig. 5). Such mean quasisteady values for immersion times up to about 3 h are shown in Table 3. It is noted that these values were more negative than that obtained for super-purity Al [15], which was −690 mV.

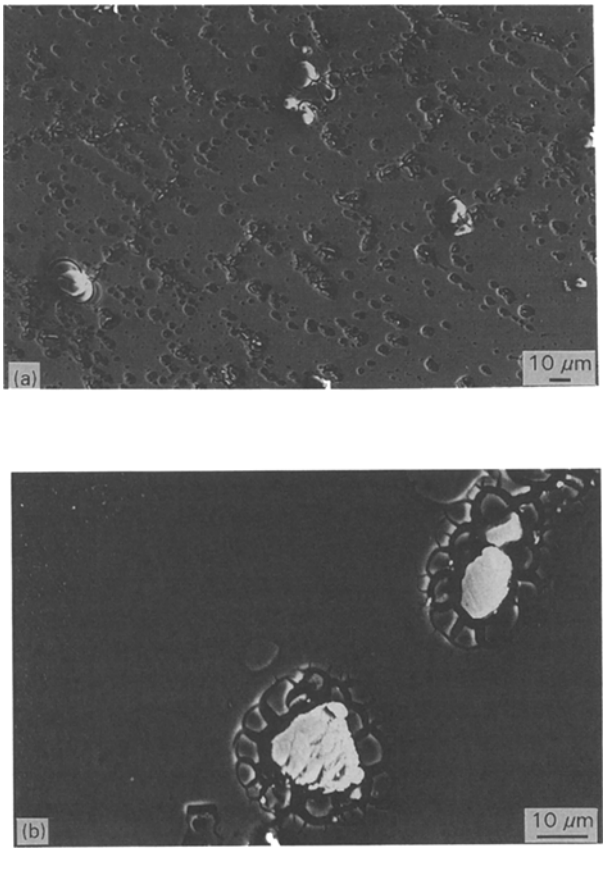

Fig. 6. SEM images of different specimens after immersion in air-saturated 0.1 M NaCl for 12 h: (a) LA and (b) JB.

All the specimens studied suffered pitting attack after a certain period of immersion in oxygen-saturated 0.1 M NaCl. As shown in Fig. 6(a), the $MgZn_2$ precipitates present in the specimens J, L and O submitted to the heat treatments A and ST disappeared from the GBs and from the inner part of the grains. It is also shown that pits developed where the $MgZn_2$ precipitates were present, this indicating that such precipitates are more easily dissolved and behave as pit nucleation centres. On certain pits, gel-like products, broken after the exposure to the high vacuum, appear. The EDX microanalysis of these products indicated the presence of aluminium chloride.

Alloys J, L and O, submitted to the heat treatments F, B and C, also presented a certain number of pits after being exposed for several hours to the oxygen-saturated 0.1 M NaCl solution (see Fig. 6(b)). However, as shown by Keller's etch, the pit nucleation centres were situated at random, appearing in the GBs and also in the inner part of the grains. This indicates that the GBs are not especially sensitive to the localized attack.

The effect of dissolved oxygen on alloys J, L and O coincides with that previously described when using alloy H submitted to the same heat treatments [15]. These results show that dissolved oxygen produces the oxidation of the alloys J, L and O up to the pitting potential (the o.c.p. rapidly increases from about −1.1 V after immersion), the sudden and frequent o.c.p. changes being ascribed to the instability of the system resulting from pitting and repassivation phenomena taking place simultaneously at different points of the metal surface. As the quasisteady condition is rapidly achieved, the mean o.c.p. does not further change despite its sudden and very frequent changes around such a mean value.

As shown in Table 3 and despite the o.c.p. fluctuations, the mean quasisteady E_{cor} potentials depended on the alloy composition. The sequence of the E_{cor} potential increase was generally in the order H < J < L < O < Al (for a given heat treatment)

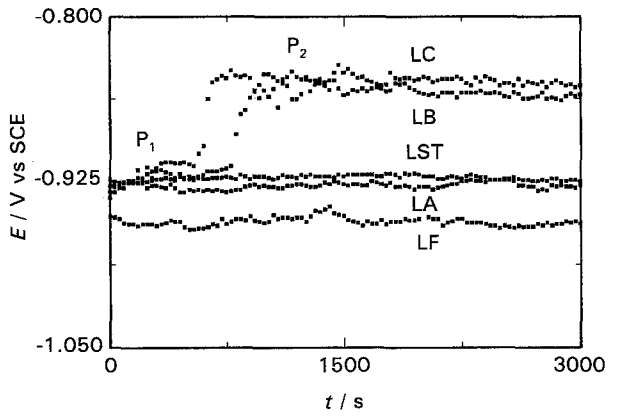

Fig. 7. (O.c.p.) against time measurements for alloy L in 1 M NaCl containing 9 ml of 30% H_2O_2 per litre of aqueous solution (G69-81) ASTM Standard Practice).

and F < A ≈ ST < B < C (for a given alloy). These sequences have to be compared with those obtained when using more aggressive electrolytes. The E_{cor} potentials were all more anodic than that measured for super purity Al and agrees with the nearly additive effect of the alloying elements when they are dissolved in solid aluminium; i.e., the Zn and Mg addition produces a shift of E_{cor} in the negative direction [1]. The Cu content, although producing a shift in the opposite direction, is not sufficient to overcome the effect of the Zn and Mg addition.

It was observed that the (o.c.p.) against time measurements were very sensitive to the oxygen dissolved. The quantity of oxygen dissolved was measured by means of an oxygen selective electrode. Although the oxygen content when measuring the o.c.p. in deaerated solutions was maintained under 0.03 ppm, it was found that an increase up to 0.15 ppm was sufficient to slowly polarize the alloys up to the o.c.p.'s measured in oxygen-saturated solutions (see Fig. 5). Such different o.c.p. values in the presence and in the absence of dissolved oxygen are related with the very different processes taking place under both conditions: oxide formation in the absence of dissolved oxygen and pitting attack in the presence of dissolved oxygen.

3.3. *Corrosion potential measurements following the G69-81 ASTM standard practice*

The E_{cor} potentials measured using the G-69-81 ASTM Standard Practice, i.e., in 1 M NaCl solution containing 9 ml of 30% H_2O_2 per litre of aqueous solution, varied with time as shown in Fig. 7. All the alloys studied in this work presented curves of the types shown in this figure. The sudden and very frequent changes found when using oxygen-saturated 0.1 M NaCl (Fig. 5) were reduced to a minimum and consequently, the E_{cor} potentials could be more accurately determined (Table 3). These values were more negative than that corresponding to 99.9995% Al, which was −780 mV. Note that the two plateaux found in H_2O_2-containing 1 M NaCl (P_1 and P_2 in Fig. 7) could not be detected in oxygen-saturated 0.1 mol dm^{-3} NaCl (Fig. 5).

The E_{cor} potentials measured in H_2O_2-containing 1 M NaCl increased in the sequences H < J < L < O < Al (for a given heat treatment) and F < A ≈ ST < B < C (for a given total composition), these sequences being also those generally obtained when using oxygen-saturated 0.1 M NaCl. The exceptions in the sequences found for the latter solution were caused by the uncertainty in the corresponding E_{cor} measurements because of the less aggressive character of the working solution and the existence of sudden, and very frequent, changes in E_{cor}. The E_{cor} potentials listed in Table 3 indicate that Cr addition to the Al–Zn–Mg alloy produces a significant shift of E_{cor} in the positive direction. The Nb addition to the Al–Zn–Mg alloy also produces a shift of E_{cor} in the positive direction, but the effect is much less marked in this case.

The result listed in Table 3 and the microscopic observation of the specimens after being immersed in H_2O_2-containing 1 M NaCl show that: (i) despite having the same total composition, specimens submitted to different heat treatments present very different corrosion potentials and differences in the form of the localized attack, proving that this technique is highly sensitive to temper and (ii) Cr and Nb additions to the Al–Zn–Mg alloy; both at the same time or independently, produce a significant shift in the E_{cor} potentials, proving that this technique is also very sensitive to small compositional changes.

Super-purity Al presented only one potential plateau because it consisted of only one homogeneous phase. The specimens F, in which, as indicated above, the $MgZn_2$ precipitates were as small as the GP zones, essentially consisted of one homogeneous phase and also presented only one potential plateau (Fig. 7). However, it is interesting to note that the alloys submitted to heat treatments A and ST presented only one plateau while they consisted of two phases, the matrix solid solution and the $MgZn_2$ precipitates. As shown previously [1], the E_{cor} potentials measured in hydrogen peroxide correspond primarily to the aluminium-rich solid solution, the predominant phase, and are not significantly affected by second-phase particles of microscopic size. On the other hand, the $MgZn_2$ precipitates suffer a very rapid attack (see Fig. 8(a)) and very different corrosion potentials are measured for alloys, H, J, L and O, submitted to the heat treatments ST and A (see Table 3). These results indicate that such corrosion potentials do not specifically correspond to the $MgZn_2$ precipitates and prove the important role of the different compositions of the matrix solid solutions produced on the alloy when adding Nb and Cr.

It was previously shown [15] that the cyclic voltammograms obtained in 0.1 mol dm^{-3} NaCl for the specimen HA presented important hysteresis (i.e., a significant difference between breakdown, E_{br}, and repassivation, E_{rp}, potentials), E_{rp} being coincident with the mean E_{cor} potential measured in the aerated

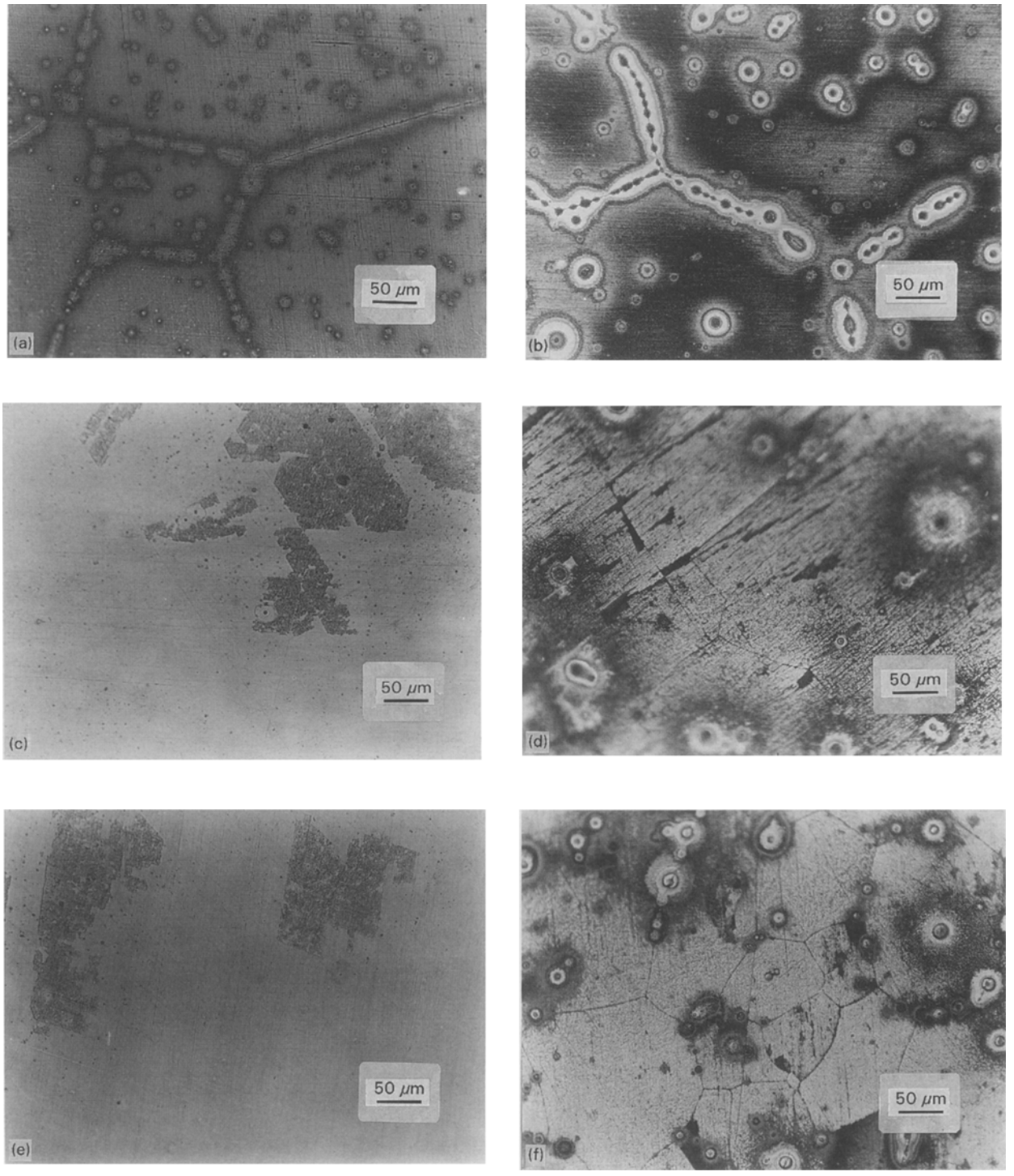

Fig. 8. Effect of the immersion of different specimens for different times in the G69-81 ASTM standard solution: (a) JA, 5 min, (b) JA, 1 h, (c) JB, 5 min, (d) JB, 1 h, (e) JC, 5 min and (f) JC, 1 h.

solution. The hysteresis was related with the size of the $MgZn_2$ precipitates, in particular in the GBs. The dissolution of these precipitates permitted the formation of rather occluded cavities at certain depth following the GBs in which the local conditions were more aggressive than in the bulk solution. Under o.c.p. conditions (this work), as $MgZn_2$ presents a pitting potential more negative than these Al–Zn–Mg alloys [15], the dissolution of such precipitates must first be produced instead of behaving as cathodic regions. Subsequently, the attack is enhanced in the resulting deep and partially occluded cavities. Note that the precipitates in the specimens A and ST are much greater than those of F, B and C (Fig. 3). This suggests a size effect of such intermetallic compounds, enhancing metal attack because their dissolution produce cavities which become partially occluded. In any case, the o.c.p.'s of the specimens A and ST are more positive than those corresponding to temper F. This agrees with the higher content in Zn and Mg of the matrix in the latter specimen, because annealing produces Zn and Mg depletion of the solid solution.

In contrast, alloys submitted to heat treatments B and C presented two plateaus, P_1 and P_2 in Fig. 7,

while, as shown by TEM, they also consisted of two phases, these being the matrix solid solution and the $MgZn_2$ precipitates. Microscopic observations carried out during the plateau P_1 in the specimens B and C (Fig. 8(c) and (e)) indicated that the corrosion points were spread over all the surface and were not localized in the GBs. The specimens B and C are produced by age-hardening of the specimen F, process in which Zn and Mg is being accumulated in the GP zones, the solid solution being partially depleted in such elements. This leads to solid solutions with compositions between those of the specimens F and A (or ST). Then, the initial plateau of the specimens submitted to heat treatments B and C, P_1 in Fig. 7, appears to be due to a surface dealloying and these specimens do not appear to be susceptible to the intergranular attack, in agreement with the previously described SCC resistance of the present Al–Zn–Mg alloys [7]. The existence of such a surface dealloying suggests that the first breakdown potential previously described for alloys H and J [11, 15, 16] also corresponds to a surface dealloying in which the intergranular region is not specifically implied. In this case, the small susceptibility to SCC of the present alloys should again be ascribed to the hydrogen embrittlement instead of the anodic dissolution, in agreement with the TEM/EDX data of the present work.

According to the data listed in Table 3, a difference of about 40 mV is found between the ASTM E_{cor} potentials of the specimens LST and HST and between those of LA and HA, while for the specimens LF and HF it is of 28 mV. As the specimens F are the most homogeneous, it appears that Cr on its own, when finely dispersed in the matrix, is able to shift E_{cor} in the positive direction. In fact, Davis *et al.* [20] proved that Cr addition to high purity Al at concentrations within the range 2–15 atom percent produced a shift of several hundreds of millivolts in the positive direction in the E_b potentials measured in 0.1 mol dm^{-3} KCl. However, it is quite insoluble in aluminium (ca. 0.05% at 500 °C in the present alloys [2]), it presents a very low diffusion coefficient in Al when compared with Cu, Zn and Mg [2] and the (Al, Cr) phase has been recognized as the direct cause of the susceptibility to quenching, that is a hardness decrease due to Mg and Zn depletion of the solid solution for slow cooling rates from the solution temperature [6]. In addition, the TEM observations indicate that the $MgZn_2$ precipitates for a given heat treatment are greater in the presence of Cr; that is, the $MgZn_2$ precipitates in the specimens LA and LST are greater than in the specimens HA and HST, while the E_{cor} potentials are more negative for the latter. As discussed above, the size of the precipitates would explain a shift of E_{corr} in the negative direction. However, the inverse shift is found when adding Cr. Consequently, the effect of Cr in the specimens A and ST must be due to its ability in shifting E_{cor} in the positive direction by itself plus its ability in nucleating the $MgZn_2$ precipitates, thus decreasing the Mg and Zn contents of the matrix solid solution with respect to the alloys which do not contain Cr. This also explains the smaller difference in the E_{cor} of the specimens HF and LF, HB and LB and HC and LC, because the high quenching rate employed to avoid quenching susceptibility limits the $MgZn_2$ nucleation on the (Al, Cr) phase and therefore the Mg and Zn depletion of the solid solution is impeded.

It is shown in Table 3 and Fig. 7 that the ASTM E_{cor} of the specimens B and C are much more positive than those of the specimens F, A and ST, while the compositions of the solid solutions of B and C do not strongly differ from those of F, A and ST. This is in agreement with the surface dealloying produced in the plateau P_1 shown in Fig. 7 and permits to interpret the further shift up to P_2 as the consequence of a Mg and Zn depletion of the solid solution, the E_{cor} being shifted in the positive direction because of such a depletion and the Cr present on the alloy surface.

The Nb addition behaves as Cr addition with respect to the E_{cor} potentials measured in chloride solutions. However, Nb was added in a lesser quantity than Cr and the E_{cor} potentials of the alloys H and J differ only in a few mV. In addition, the sizes of the $MgZn_2$ precipitates in the specimens JA and JST are smaller than those found in the specimens LA and LST. This indicates that the Nb effect is essentially due to its presence in solid solution. When comparing the ASTM E_{cor} values of the alloys L and O, differences of a few millivolt are only found. This indicates the predominant effect of Cr, the effects of Cr and Nb being additive.

The results shown in Table 3 also permit prediction of the effect of Cr and Nb on the pitting corrosion resistance of these alloys. In fact, the presence of a strong oxidizing agent leads to the polarization of these Al–Zn–Mg alloys to pitting conditions, the corresponding potential being coincident with the E_{rp} potential measured from the cyclic voltammograms [11, 15, 16]. As shown for alloys H and J, the sequence in E_{rp}, the relevant quantity in pitting studies instead of E_b [11, 15, 16], coincides with the E_{cor} sequence. This suggests that the pitting resistance of the present Al–Zn–Mg alloys also increases in the ASTM E_{cor} order H < J < L < O. The general result is that Cr and Nb increases the pitting corrosion resistance of alloy H, their effects being additive, the effect of Cr being dominant at the concentrations studied in this work.

4. Conclusions

The electron microscopic observations showed the inclusion of Cu in the $MgZn_2$ precipitates formed during annealing (A), cold-rolling (ST) and ageing (B and C) Al–5%Zn–1.67%Mg–0.23%Cu and Al–5%Zn–1.67%Mg–0.24%Cu–0.14%Cr. In addition, Cr was also detected in a greater quantity in the $MgZn_2$ precipitates found in aged Al–5%Zn–1.67%Mg–0.24%Cu–0.14%Cr. The EDX microanalysis of the precipitate free zones of the age-hardened specimens

(B and C) did not show significant compositional differences from those corresponding to the matrix solid solutions.

The annealed, quenched and cold-rolled specimens presented only one corrosion potential plateau in H_2O_2-containing 1 M NaCl despite consisting of two phases, the $MgZn_2$ precipitates and the matrix solid solution. Two corrosion potential plateaus were found for the age hardened Al–Zn–Mg alloys in the same electrolyte. Intergranular attack was not evident after the first plateau, but a surface transformation affecting all the grain due to a surface dealloying.

The presence of oxygen dissolved in chloride solutions is able to polarize the present Al–Zn–Mg alloys up to a potential in which pitting corrosion takes place. The cavities formed where such precipitates were present behave as pit nucleation centres in the case of the annealed (A) and cold-rolled (ST) specimens because their size favour the formation of aggressive local environments.

The corrosion potentials in oxygen-saturated or H_2O_2-containing chloride solutions strongly depended on the composition of the matrix solid solution; i.e., the predominant phase of the alloy. Such corrosion potential measurements were highly sensitive to the composition of the alloys and heat treatments. The E_{cor} potentials measured in oxygen-saturated 0.1 mol dm^{-3} NaCl and in H_2O_2-containing 1 M NaCl increased in the sequence H < J < L < O < Al (for a given heat treatment) and F < A ≈ ST < B < C (for a given total composition).

The present compositional determinations and corrosion potential measurements together with the corresponding microscopic observations indicate that the pitting corrosion resistance increased with Cr and Nb addition. The effects of both were additive although the effect of the latter was less marked. On the other hand, the present results are consistent with the previously found SCC resistance of the Al–Zn–Mg alloys studied, their small susceptibility being probably due to hydrogen embrittlement.

Acknowledgements

The authors gratefully acknowledge the financial support of this work by the DGICYT (Spain), project No. PB91-0260 and the grant conceded to A. H. Moreira by the CNPq (Brazil). The authors also thank the 'Servei Científico-Tècnic de la Universitate de Barcelona' for the facilities in the SEM, TEM, STEM observations and EDX microanalysis. The authors are also indebted to W. Gárlipp and M. Cilense for the preparation of the alloys.

References

[1] 'Corrosion', *in* 'Metals Handbook', 9th edn, vol. 13, ASM, Metals Park, OH (1987) pp. 583–609.
[2] L. F. Mondolfo, *Metall. Rev.* **16** (1971) 95.
[3] S. C. Byrne, *in* 'Aluminium Alloys. Physical and Mechanical Properties', vol 2, (edited by E.A. Stark and T.H. Sanders), Warley, UK (1986) pp. 1095–1107.
[4] H. Cordier, C. Dumont and W. Gruhl, *Aluminium* **55** (1979) 777.
[5] H. Cordier, C. Dumont and W. Gruhl, *Metall.* **34** (1980) 515.
[6] H. Cordier, C. Dumont, W. Gruhl and B. Grzemba, *ibid.* **36** (1982) 33.
[7] W. Gárlipp, S. Saimoto and H. M. dos Santos, Proceedings of the meeting of the Associação Brasileira de Metais, Belo Horizonte, Minas Gerais, Brazil (1987) pp. 33–44.
[8] S. Maitra and G. C. English, *Metall. Trans.* **12A** (1981) 535.
[9] I. J. Polmear, *J. Inst. Metals* **89** (1960–61) 51.
[10] M. Cilense, PhD. thesis, Araraquara, Brazil (1990).
[11] P. L. Cabot, A. H. Moreira, J. A. Garrido, P. T. A. Sumodjo, E. Pérez and W. Proud, *Electrochim. Acta* **40** (1995) 447.
[12] J. R. Galvele and S. M. de Micheli, *Corros. Sci.* **10** (1970) 795.
[13] H.-P. Kim, R.-H. Song and S.-I. Pyun, *Br. Corros. J.* **23** (1988) 254.
[14] G. M. Scamans, N. J. H. Holroyd and C. D. D. Tuck, *Corros. Sci.* **27** (1987) 329.
[15] P. L. Cabot, F. Centellas, J. A. Garrido, R. M. Rodríguez, E. Brillas, E. Pérez, A. V. Benedetti and P. T. A. Sumodjo, *J. Appl. Electrochem.* **22** (1992) 541.
[16] P. L. Cabot, F. Centellas, E. Pérez and R. Loukili, *Electrochim. Acta* **38** (1993) 2741.
[17] Th. Hehemkamp, *in* 'Solute-Defect Interaction: Theory and Experiment', (edited by S. Saimoto, G. R. Purdy and G. V. Kidson), Pergamon, Toronto, Canada (1986) pp. 241–250.
[18] 'Metallography and Microstructures', *in* 'Metals Handbook', 9th edn, vol. 9, ASM, Metals Park, OH (1985) pp. 351–360.
[19] G. D. Davis, W. C. Moshier, J. S. Ahenarn, H. F. Hough and G. O. Cote, *J. Vac. Sci. Technol. A* **5** (1987) 1152.
[20] G. D. Davis, W. C. Moshier, T. L. Fritz and G. O. Cote, *J. Electrochem. Soc.* **137** (1990) 422.